coatings

MDPI

Article

A Cost-Effective, Nanoporous, High-Entropy Oxide Electrode for Electrocatalytic Water Splitting

Bu-Jine Liu [1,†], Tai-Hsin Yin [1,†], Yu-Wei Lin [1], Chun-Wei Chang [1], Hsin-Chieh Yu [1], Yongtaek Lim [2], Hyesung Lee [2], Changsik Choi [2,*], Ming-Kang Tsai [3] and YongMan Choi [1,*]

[1] College of Photonics, National Yang Ming Chiao Tung University, Tainan 71150, Taiwan; bujine.c@nycu.edu.tw (B.-J.L.); taihsin.pt09@nycu.edu.tw (T.-H.Y.); ywlin0911.pt09@nycu.edu.tw (Y.-W.L.); winerchang7.pt10@nycu.edu.tw (C.-W.C.); hcyu@nycu.edu.tw (H.-C.Y.)
[2] Clean Energy Conversion Research Center, Institute for Advanced Engineering, Yongin 17180, Republic of Korea; ytlim@iae.re.kr (Y.L.); hslee@iae.re.kr (H.L.)
[3] Department of Chemistry, National Taiwan Normal University, Taipei 11677, Taiwan; mktsai@ntnu.edu.tw
* Correspondence: cschoi@iae.re.kr (C.C.); ymchoi@nycu.edu.tw (Y.C.)
† These authors contributed equally to this work.

Abstract: High-entropy materials have attracted extensive attention as emerging electrode materials in various energy applications due to their flexible tunability, unusual outstanding activities, and cost-effectiveness using multiple earth-abundant elements. We introduce a novel high-entropy composite oxide with the five elements of Cu, Ni, Co, Fe, and Cr (HEO-3CNF) for use in the oxygen evolution reaction (OER) in electrocatalytic water splitting. HEO-3CNF is composed of two phases with a non-equimolar, deficient high-entropy spinel oxide of $(Cu_{0.2-x}Ni_{0.2}Co_{0.2}Fe_{0.2}Cr_{0.2})_3O_4$ and monoclinic copper oxide (CuO). Electrochemical impedance spectroscopy (EIS) with distribution of relaxation times (DRT) analysis validates that the HEO-3CNF-based electrode exhibits faster charge transfer than benchmark CuO. It results in improved OER performance with a lower overpotential at 10 mA/cm^2 and a Tafel slope than CuO (518.1 mV and 119.7 mV/dec versus 615.9 mV and 131.7 mV/dec, respectively) in alkaline conditions. This work may provide a general strategy for preparing novel, cost-effective, high-entropy electrodes for water splitting.

Keywords: hydrogen production; high-entropy oxides; electrochemical impedance spectroscopy; thin films

Citation: Liu, B.-J.; Yin, T.-H.; Lin, Y.-W.; Chang, C.-W.; Yu, H.-C.; Lim, Y.; Lee, H.; Choi, C.; Tsai, M.-K.; Choi, Y. A Cost-Effective, Nanoporous, High-Entropy Oxide Electrode for Electrocatalytic Water Splitting. *Coatings* **2023**, *13*, 1461. https://doi.org/10.3390/coatings13081461

Academic Editor: Cristiana Alves

Received: 3 August 2023
Revised: 14 August 2023
Accepted: 17 August 2023
Published: 19 August 2023

1. Introduction

Limited availability of fossil fuels and climate change have necessitated a search for novel, high-efficient, and sustainable green energy technologies. Numerous green technologies have been widely developed, such as solar energy generation [1,2], wind power generation [3], and hydroelectric power generation [4]. In addition to developing different power generation methods and reducing environmental risks from traditional energy sources, the rational design of novel electrode materials and efficient energy storage systems is crucial due to intermittent power generation using renewable energy sources [5]. Although green hydrogen production from renewable energy sources is considered a promising approach for net-zero carbon emissions [6,7], ~95% of global hydrogen production is based on fossil fuels [8] (i.e., gray or brown hydrogen), releasing carbon emissions [9]. Hence, developing high-efficiency green hydrogen production technologies from water (i.e., electrochemical [10] and photoelectrochemical (PEC) water electrolysis [11,12]) is imperative. In particular, developing novel high-performance electrode materials for the oxygen evolution reaction (OER) for electrochemical and PEC water electrolysis has attracted much attention because its sluggish reaction kinetics retard large-scale hydrogen production [13]. Recently, the high-entropy concept has been widely applied for designing novel better materials (i.e., high-entropy alloys) [14] and expanded to develop numerous emerging

energy materials in water splitting [15] and supercapacitors [16]. High-entropy materials are formed by mixing equimolar [17] or non-equimolar [14] ratios of ≥five different elements. To date, different types of high-entropy materials have been introduced in the literature, such as high-entropy alloys (HEAs) [14], high-entropy nitrides (HENs) [18–20], high-entropy carbides (HECs) [21], and high-entropy oxides (HEOs) [22–24]. HEOs have demonstrated unexpected, remarkable properties for narrow band gaps [25], colossal dielectric constants [23], and enhanced mechanical properties [26]. In this study, to select five elements for HEO electrode materials, a fundamental concept of elements was applied, including similar crystal structures, geometric compatibility, and oxidation states [27], similar to previous studies in supercapacitors [28], Li-ion batteries [29], and fuel cells [30]. In addition, we initiated HEO preparation based on monoclinic CuO (space group *C2/c*) [31], which is widely used in PEC water splitting [32], to search for cost-effective electrode materials. Then, we selected four cost-effective, earth-abundant elements: Ni, Co, Fe, and Cr. Although they are widely used in HEA applications [33–36], to our knowledge, applying this combination of HEOs in energy applications (i.e., water electrolysis) has not received much attention. Accordingly, in this study, we investigated their physical and electrochemical properties after making thin-film electrodes using the drop-casting method. We also examined their electrochemical double-layer capacitance (C_{dl}) and OER activity for viable applications in electrocatalytic green hydrogen production. In addition to the electrode material design, the substrates (i.e., metal foils [37], metal foams [38], carbon cloths [39], and transparent conductive films [40]) play a pivotal role in accurate and effective performance measurements at the lab scale. We applied fluorine-doped tin oxide-coated glass (FTO), since it can be effectively employed as an electrode substrate in photoelectrochemical (PEC) water splitting [41–43] due to excellent compatibility with other conductive substrates for further practical applications [44] and crystallinity with a zig-zag surface suitable for homogeneous deposition [45].

2. Experimental Details

2.1. Preparation of High-Entropy Oxides and Fabrication of Electrodes

As shown in Figure 1, a high-entropy oxide with the five elements of Cu, Ni, Co, Fe, and Cr (HEO-3CNF) was synthesized using a citrate method. The nominal composition of $Cu(NO_3)_3{\cdot}6H_2O$, $Ni(NO_3)_2{\cdot}6H_2O$, $Co(NO_3)_2{\cdot}6H_2O$, $Fe(NO_3)_2{\cdot}6H_2O$, and $Cr(NO_3)_3{\cdot}6H_2O$ (Alfa Aesar and ACROS, MA, USA) were mixed stoichiometrically with citric acid (SIGMA-ALDRICH, Burlington, MA, USA) in deionized (DI) water. A sol-gel was formed by stirring and heating at 90 °C in an oven for 6 h. Subsequently, the gel was dried at 400 °C for 2 h and calcined at 700 °C for 3 h in air in a tube furnace (Thermo Scientific, Lindberg Blue M, Waltham, MA, USA) with a heating rate of 10 °C/min to obtain HEO-3CNF powders. HEO-3CNF powders were ground in an agate mortar for further characterization. As mentioned, CuO (Alfa Aesar, Haverhill, MA, USA) was used as a parent phase to evaluate the crystal structures of HEO-3CNF powders and benchmark. As depicted in Figure 1, thin-film electrodes were fabricated using the drop-casting method after preparing a slurry with terpineol (Alfa Aesar, Haverhill, MA, USA), ethyl cellulose (SIGMA-ALDRICH, Burlington, MA, USA), and acetic acid with a weight ratio of 1:6:0.5:0.1. It is noted that ethyl alcohol was added to obtain the proper viscosity for drop casting on FTO substrates. FTO substrates were cleaned with acetone, isopropanol, ethyl alcohol, and DI water with an ultrasonic cleaner for 5 min, then dried in an oven. The active electrode area was fixed at 1.0 cm^2 with a chemical-tolerant tape. After dropping the slurry and carefully removing the tape, the fabricated electrodes were placed in a high-temperature oven (Panchum, Kaohsiung, Taiwan) at 400 °C for 30 min to remove organics. CuO and IrO_2 powders (Alfa Aesar, Haverhill, MA, USA) were used as a reference to evaluate the OER activity.

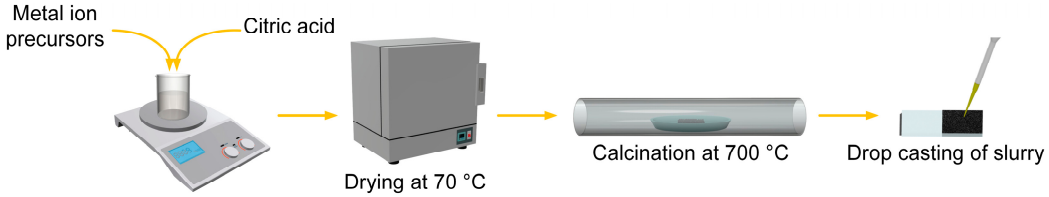

Figure 1. Schematic illustration of the synthesis of HEO-3CNF powders using a citrate method and fabricating electrodes on FTO using the drop-casting method. The slurry is a mixture of HEO-3CNF, terpineol, ethyl cellulose, acetic acid, and ethyl alcohol.

2.2. Characterization of Electrode Materials

The crystal structure of HEO-3CNF powders was examined via X-ray diffraction (XRD, Brucker D8 DISCOVER, Billerica, MA, USA) with Cu Kα radiation (λ = 0.154184 nm) in the range of 10–80°. An X-ray photoelectron spectrometer (XPS, Thermo Scientific K-Alpha, Waltham, MA, USA) was applied using Al Kα radiation. Scanning electron microscopy (SEM, Zeiss Gemini 450, Jena, Germany) was used to examine the surface morphology. An inductively coupled plasma-mass spectrometer (ICP-MS, Thermo fisher scientific iCAP TQ, Waltham, MA, USA) was used to investigate the molar ratio of HEO-3CNF powders. As-prepared HEO-3CNF powders were dissolved in the aqua regia and hydrofluoric acid with the microwave digestion method. The solution was heated with the microwave digestion system (CEM MARS 6, Matthews, NC, USA) for 1 h at ~180 °C. Electrochemical property measurements, including cyclic voltammetry (CV), linear sweep voltammetry (LSV), and electrochemical impedance spectroscopy (EIS), were carried out using a potentiostat (SP-150e, BioLogic, Seyssinet-Pariset, France). Thin-film electrodes prepared on FTO with HEO-3CNF, CuO, and IrO_2 were applied as the working electrode, while a graphite rod was used as the counter electrode. Hg/HgO was used as the reference electrode in 1.0 M KOH. The Nernst equation was used to convert different reference potentials to the reversible hydrogen electrode (RHE), $V_{RHE} = V^0_{Ref} + 0.059 \times pH + V_{Ref}$, where V_{RHE} is the converted potential in RHE, pH is the pH value of the electrolyte, V_{ref} is the measured potential against the reference electrode, and V^0_{Ref} is the constant for Hg/HgO (0.098). EIS measurements were conducted from 100 kHz to 10 mHz with 5 mV sinusoidal amplitude with six data points per frequency decade to examine CuO and HEO-3CNF electrodes deposited on FTO. In this study, polarization curves were measured at the scan rate of 5 mV/s after conditioning the working electrode at 100 mV/s. The overpotential (η) was calculated at 10 mA/cm^2 by $\eta = E_{RHE} - 1.23$ at ambient temperature. The Tafel slope (A) was obtained using the Tafel equation of $\eta = A \cdot \log(j) + B$. The double-layer capacitance (C_{dl}) was obtained by continuously measuring CVs at scan rates of 10, 25, 50, 75, and 100 mV/s in the double-layer region (a non-Faradic, OER potential range).

3. Result and Discussion

3.1. Characterization of High-Entropy Oxides

Figure 2a shows a Rietveld refinement of XRD patterns of HEO-3CNF powders, exhibiting the distinctive diffraction peaks at 18.5°, 30.5°, 35.9°, 37.5°, 38.8°, 43.6°, 48.7°, 54.2°, 57.8°, 63.5°, and 75.2°. The peaks at 18.5°, 30.5°, 35.9°, 37.5°, 43.7°, 54.3°, 63.5°, and 75.3° are matched well with the spinel phase (COD ID: 1533162) [46], and those at 35.9°, 38.8°, and 68.2° can be assigned to the monoclinic phase (COD ID: 1011148) [47]. The lattice parameters of the oxides of various metal cations that make up HEO-3CNF are shown in Table S1 [48–52] to investigate and understand the lattice structure of HEO-3CNF. It was reported that HEO materials could exist as a multiphase composite [53–55], similar to our nanoporous synthesis condition at 700 °C. Then, the Rietveld refinement analysis was performed using the FullProf Software suite [56]. The initial phase information was obtained from the Crystallography Open Database [57]. It resulted in the R-pattern (R_p) parameter of 5.19%, R-weighted pattern (R_{wp}) parameter of 7.16%, and χ^2 of 1.03, indicating acceptable refinement results. Based on the refinement result, we confirmed that HEO-

3CNF powders consist of the 78.5% spinel phase ($Fd\bar{3}m$, a = b = c = 8.2681 Å, α = β = γ = 90°) and the 21.5% monoclinic phase (*C2/m*, a = 4.6817 Å, b = 3.4155 Å, c = 5.1215 Å, α = γ = 90°, β = 99.4°). The refinement parameters of the HEO-3CNF composite were summarized and shown in Table S2. Besides, the crystal size of the HEO-3CNF powders was calculated using the Debye–Scherrer relation (Equation (1)), and the average crystallite size was ~47.61 nm.

$$D = \frac{K\lambda}{\beta \cos \theta} \quad (1)$$

where D is the average crystal size, K is the Scherrer constant (0.9), λ is the wavelength of the incident X-ray, β is the full-width half maximum value, and θ is the Bragg angle.

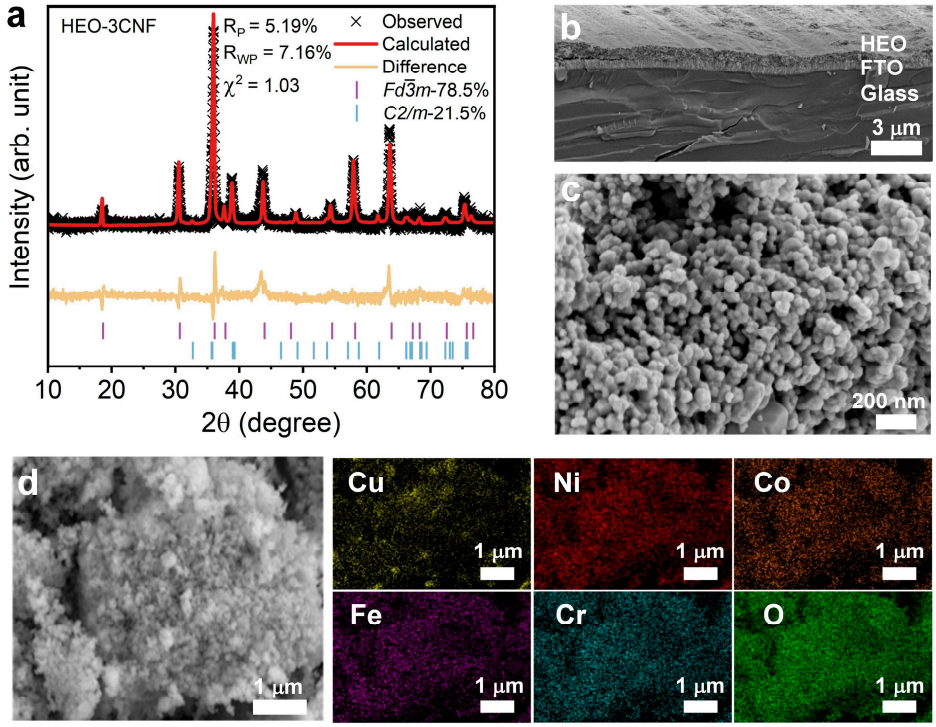

Figure 2. (**a**) Rietveld refinement of XRD patterns, (**b**) side view, and (**c**) enlarged view of HEO-3CNF-based electrodes on FTO using the drop-casting method, and (**d**) SEM image used for EDS analysis and EDS mapping results for as-prepared HEO-3CNF powders.

Figure 2b–d demonstrate representative SEM images of the prepared electrode and HEO-3CNF powders. The side and enlarged views of the HEO-3CNF electrode are shown in Figure 2b,c, exhibiting the HEO-3CNF thin film uniformly coated on the FTO substrate. The thickness of the HEO-3CNF thin film was around ~800 nm (Figure 2b). Figure 2c illustrates the morphology of the electrode at the nanoscale, confirming the nanoporous structure with a particle size of 58.7 ± 14.5 nm (Figure S1). Figure 2d shows an SEM image of as-prepared HEO-3CNF powders used for the energy-dispersive X-ray spectroscopy (EDS) analysis used to verify the element distribution of HEO-3CNF at the nanoscale. The five elements of Cu, Ni, Co, Fe, and Cr are uniformly distributed, as presented in Figure 2d. Furthermore, to precisely examine the equimolar ratio of HEO-3CNF, ICP-MS was applied, as shown in Table S3. Then, we performed high-resolution XPS analysis (Figure 3) to investigate the element composition further and confirm the chemical state. Figure S2 shows the XPS full survey spectrum, while Figure 3a demonstrates the O 1s spectrum. The peaks are attributed to lattice oxygen in metal oxide (O_L) and vacancy oxygen (O_V) (529.6 and 530.6 eV, respectively [58]). Oxygen vacancies are generated to maintain the electroneutrality of the crystal structure of the sample using five metal elements with different oxidation states, as shown in Figure 3b–f. We assumed that oxygen vacancies

could play a vital role in the electrochemical performance of HEO-3CNF electrodes [59]. For Cu 2p, its deconvolution was performed, as displayed in Figure 3b. The peaks at 933.5 eV (Cu $2p_{3/2}$) and 953.7 eV (Cu $2p_{1/2}$) can be assigned to Cu^{2+} [60]. Furthermore, we observed that the shake-up satellite peak is at 945.7 eV and proved the existence of CuO [61,62]. Figure 3c shows the Ni 2p XPS spectrum with two spin-orbit peaks. Ni $2p_{3/2}$ can be further deconvoluted into Ni^{2+} (854.2 eV) and Ni^{3+} (855.6 eV), and Ni $2p_{1/2}$ into Ni^{2+} (871.7 eV) and Ni^{3+} (873.6 eV) [63]. The Co 2p XPS spectrum is displayed in Figure 3d, resulting in Co^{3+} at 779.7 eV (Co $2p_{3/2}$) and 794.8 eV (Co $2p_{1/2}$), and Co^{2+} at 780.5 eV (Co $2p_{3/2}$) and 796.5 eV (Co $2p_{1/2}$) [64,65]. Figure 3e illustrates the Fe 2p spectrum composed of two spin-orbit peaks and a satellite peak. The peaks at 712.0 eV (Fe $2p_{3/2}$) and 725.9 eV (Fe $2p_{1/2}$) are related to Fe^{3+}, and those at 710.0 eV (Fe $2p_{3/2}$) and 722.5 eV (Fe $2p_{1/2}$) are associated with Fe^{2+} [66]. Figure 3f demonstrates the Cr 2p spectrum. While the peaks at 575.9 eV (Cr $2p_{3/2}$) and 585.5 eV (Cr $2p_{1/2}$) are attributed to Cr^{3+}, those at 578.5 eV (Cr $2p_{3/2}$) and 587.8 (Cr $2p_{1/2}$) are assigned to Cr^{6+} [65,67].

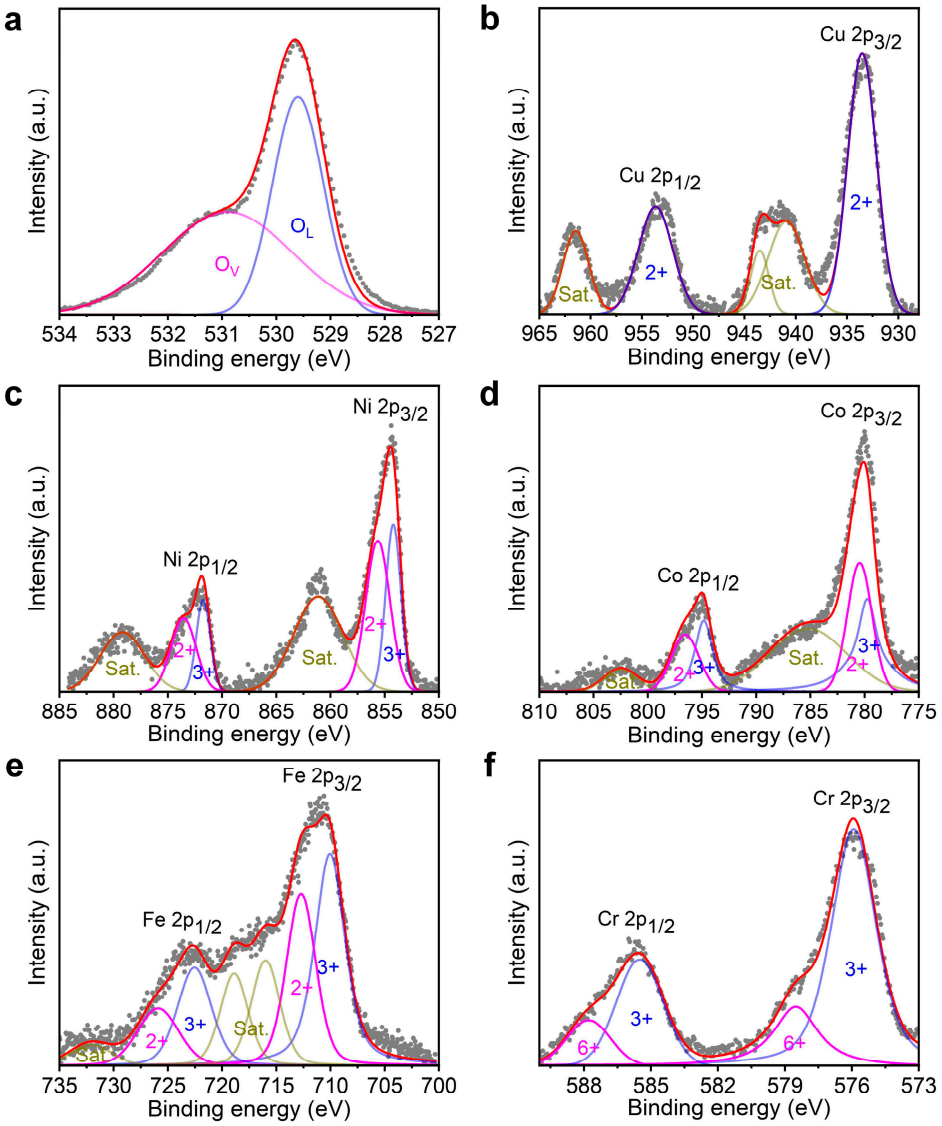

Figure 3. High-resolution XPS analysis for HEO-3CNF powders. Deconvoluted XPS spectra of (**a**) O 1s, (**b**) Cu 2p, (**c**) Ni 2p, (**d**) Co 2p, (**e**) Fe 2p, and (**f**) Cr 2p Dots (gray) and lines (red) are the measured data and fitted results. Deconvoluted lines represent different oxidation states (blue and pink) and satellite peaks (olive).

3.2. Electrochemical Impedance Studies of High-Entropy Metal Oxide Electrodes

EIS measurements were first carried out to investigate the electrical properties of the electrodes further. The Nyquist plots of the CuO and HEO-3CNF electrodes in the Ar-purged 1.0 M KOH electrolyte are shown in Figure 4a,b. The electrical equivalent circuit (EEC) model to fit the impedance data is also illustrated in Figure 4a, including the system resistance (R_s), charge transfer resistance (R_{ct}), constant phase element (CPE), Warburg impedance (W), and pseudocapacitance capacitance (C). EIS spectra (Figure 4a,b) exhibit a stable slope for CuO at 11.49–0.99 Hz and HEO-3CNF at 7.68–0.99 Hz, denoting reflection boundary conditions of Warburg elements [68,69]. Table 1 compiles the fitting parameters of each circuit component for CuO and HEO-3CNF electrodes. The HEO-3CNF (R_{ct} = 18.7 Ω) [70–72] electrode has a lower charge transfer resistance with a capacitance value than the CuO (R_{ct} = 2.7 × 10^4 Ω) [73,74] electrode, denoting easier ion access on the HEO-3CNF electrode/electrolyte interface [75]. It also indicates enhanced capacitance [76] and OER activity [77] of HEO-3CNF compared to CuO. Meanwhile, the pseudocapacitance of CuO (C = 6.4 × 10^{-5} F) is much lower than that of HEO-3CNF (C = 2.6 × 10^{-3} F), potentially resulting in the better capacitance of HEO-3CNF than CuO [78]. The capacitance formed by the semicircular charge transfer mechanism is not apparent at the high frequency of EIS, and it is replaced by CPE to investigate the current distribution on electrode surfaces. α can be used to characterize the capacitive response of the electrode material. According to its value of 0.92 to 0.80 (Table 1), the two electrodes show a pseudocapacitive response [79]. In addition, we carried out a distribution of relaxation times (DRT) analysis that defines the physical processes as an infinite series of RC circuits represented by a distribution function in the time domain [80]. The DRT method can be applied to analyze the electrochemical reaction process at each frequency decade [81–83]. As shown in Figure 4c,d, the DRT plot consists of three types of peaks, which can be characterized by different polarization processes based on relaxation time (τ), including series resistance and active material resistance in the high-frequency (HF) region (low τ), charge transfer resistance in the middle-frequency region (MF) (middle τ), interactions of the electrode interface/electrolyte, and the influence of Warburg impedance in the low-frequency (LF) region (high τ) [84]. Figure 4c,d show the DRT analysis resulting in distinctive peaks for the CuO (τ = 2.49 × 10^{-3} s with $\gamma(\tau)$ = 643.3 Ω) and HEO-3CNF (τ = 2.37 × 10^{-3} s with $\gamma(\tau)$ = 16.3 Ω) electrodes. Due to the high time constant in the low-frequency (LF) region, the highest peak intensity in the DRT spectrum can be interpreted as the diffusion of ions [85]. The peak of CuO in the LF region shifts to a higher time constant, indicating that the diffusion of CuO ions becomes slower compared to HEO-3CNF. At the same time, the lower peak intensity of HEO-3CNF ($\gamma(\tau)$ = 16.3 Ω) than CuO ($\gamma(\tau)$ = 643.3 Ω) demonstrates its better catalytic performance and conductivity [84], which agrees with the R_{ct} values in the Nyquist plots (Figure 4a,b). The DRT analysis of CuO (τ = 9.84 × 10^{-5} s with $\gamma(\tau)$ = 74.9 Ω) in the mid-frequency (MF) region indicate a less efficient charge transfer than HEO-3CNF (τ = 1.92 × 10^{-4} s with $\gamma(\tau)$ = 6.1 Ω). It can be verified with the R_{ct} value using the EEC model. In the high-frequency (HF) region, CuO (τ = 1.47 × 10^{-5} s with $\gamma(\tau)$ = 15.7 Ω) shows a higher peak than HEO-3CNF (τ = 2.46 × 10^{-4} s with $\gamma(\tau)$ = 3.8 Ω), owing to the higher resistance [86]. In summary, the EIS analysis with the DRT method verified the faster charge transfer and better capacitance performance of the HEO-3CNF electrode than the CuO electrode.

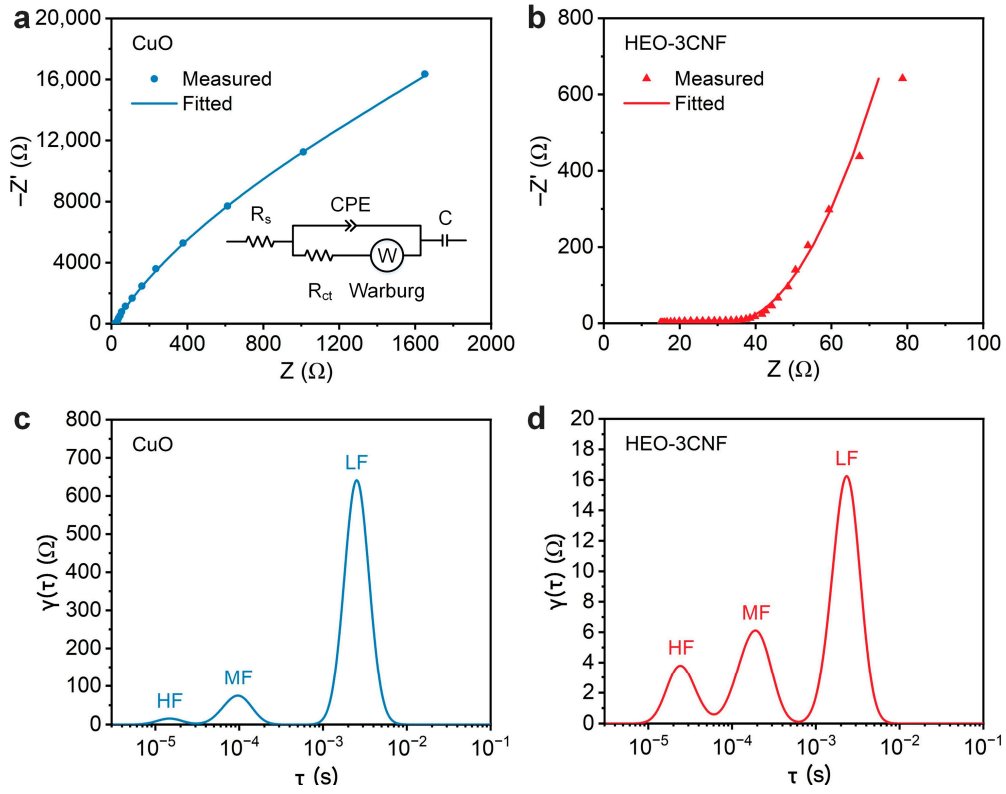

Figure 4. Electrochemical impedance spectra for (**a**) CuO and (**b**) HEO-3CNF-based electrodes and corresponding DRT curves (**c**) and (**d**). The EEC model used to fit the impedance data is shown. Ar-saturated solutions were used.

Table 1. EIS fitting parameters of CuO and HEO-3CNF electrodes.

Electrode	R_s (Ω)	R_{ct} (Ω)	Q ($F \times s^{(\alpha - 1)}$)	α	CPE (F)	W ($\Omega/s^{1/2}$)	C (F)
CuO	16.1	2.7×10^4	1.3×10^{-4}	0.92	1.4×10^{-4}	1169	6.4×10^{-5}
HEO-3CNF	15.7	18.7	1.2×10^{-4}	0.80	2.6×10^{-5}	30.4	2.6×10^{-3}

3.3. Electrochemical Measurements of High-Entropy Metal Oxide Electrodes

After the characterization of HEO-3CNF, we investigated its potential applications in water electrolysis (Figure 5). Figure 5a,b show CV results of the HEO-3CNF and CuO electrodes at different scan rates, indicating the presence of electric double-layer capacitance. The scan-rate-dependent increase in integrated areas describes the possibility of reacting with electrolytes. The double-layer capacitance (C_{dl}) was calculated by plotting the current density and scan rate at a selected potential. As shown in Figure 5c, HEO-3CNF has a much better capacitive capability for potential supercapacitors than CuO. Then, the applicability of HEO-3CNF for electrocatalytic water splitting was examined by measuring OER activities. As summarized in Figure 5d, the iR-corrected polarization curve [87] of HEO-3CNF was compared with those of CuO and IrO_2. The overpotentials at 10 mA/cm^2 of IrO_2, HEO-3CNF, and CuO are 351.9, 518.1, and 615.9 mV (Figure 5e), which agree with previous results (IrO_2: 351 mV and CuO: 580 mV) [88,89]. Shown in Figure 5f are their Tafel slopes with 75.2, 119.7, and 131.7 mV/dec. As reported, multi-phase catalysts can increase active adsorption sites and boost charge transfer between catalyst surfaces and adsorbents [90,91], leading to higher OER performance. This study demonstrated that the novel HEO-3CNF-based OER electrodes enhance their performance compared to CuO, which can be applied in various energy devices (i.e., supercapacitors and alkaline water electrolyzers).

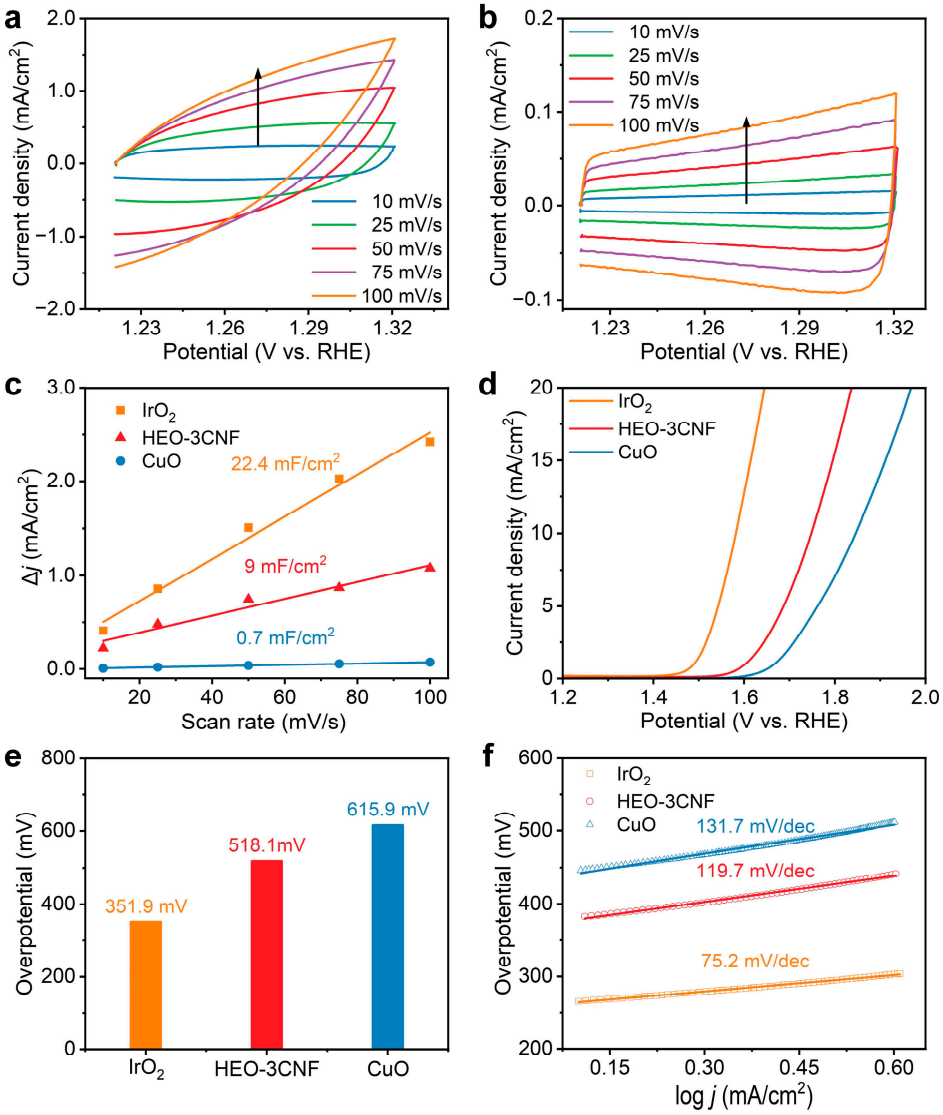

Figure 5. CVs at different scan rates (10, 25, 50, 75, and 100 mV/s) in 1.0 M KOH for (**a**) HEO-3CNF and (**b**) CuO electrodes. (**c**) Relation of the current against the scan rates to estimate double-layer capacitance (C_{dl}) in a non-faradaic range of 0.89–0.9 V (IrO_2), 1.24–1.26 V (CuO), and 1.25–1.26 V (HEO-3CNF). OER activity measurements of IrO_2, HEO-3CNF, and CuO in 1.0 M KOH. (**d**) LSV polarization curves, (**e**) overpotentials measured at 10 mA/cm^2, and (**f**) Tafel slopes. CV and LSV measurements were performed in an Ar-saturated solution, while OER measurements were in an O_2-saturated solution. The potentials are iR-corrected.

4. Conclusions

A high-entropy composite with spinel and monoclinic phases was synthesized using a citrate acid method at 700 °C as the OER electrode for electrocatalytic water splitting. Various characterization approaches verified the equimolar high-entropy oxide and its composite formation. In particular, the EIS analysis with the DRT method clarified faster charge transfer and better capacitance performance of the HEO-3CNF electrode than the CuO electrode. The two-phase heterostructure improved the OER activity under alkaline conditions compared to CuO, with the overpotentials at 10 mA/cm^2 of 518.1 mA and 615.9 mA, respectively. In addition, we observed that the Tafel slope of the HEO-3CNF electrode (119.7 mV/dec) is lower than that of the CuO electrode (131.7 mV/dec). Its comparison with previous studies is compiled in Table S4 [92,93]. This work may provide a general strategy for preparing novel, cost-effective, high-entropy electrodes for water splitting, as well as for use as energy storage materials.

Supplementary Materials: The following supporting information can be downloaded at: https://www.mdpi.com/article/10.3390/coatings13081461/s1, Table S1: Lattice parameters of different metal oxides, Table S2: Refinement parameters of the HEO-3CNF composite, Table S3: The atomic ratio of five elements in as-synthesized HEO-3CNF, Table S4: OER performance of HEO electrodes. Figure S1: Particle size distribution of HEO-3CNF powders, Figure S2: XPS full survey spectrum of HEO-3CFN powders.

Author Contributions: Conceptualization, Y.C.; methodology, B.-J.L., T.-H.Y., Y.-W.L. and C.-W.C.; software, B.-J.L. and T.-H.Y.; investigation, B.-J.L., T.-H.Y., Y.-W.L. and C.-W.C.; data curation, T.-H.Y., Y.-W.L. and C.-W.C.; visualization, T.-H.Y. and Y.-W.L.; writing—original draft preparation, B.-J.L., T.-H.Y., Y.-W.L. and C.-W.C.; writing—review and editing, H.-C.Y., Y.L., H.L., C.C., M.-K.T. and Y.C.; supervision, Y.C.; project administration, Y.C. All authors have read and agreed to the published version of the manuscript.

Funding: This research was funded by the National Science and Technology Council of Taiwan (NSTC Grant No. 110-2221-E-A49-017-MY3). C.C. thanks the Ministry of Trade, Industry, and Energy (MTIE) of Korea for the Net-Zero Demand Management Program (KETEP 20212010200110).

Institutional Review Board Statement: Not applicable.

Informed Consent Statement: Not applicable.

Data Availability Statement: Not applicable.

Acknowledgments: We acknowledge the Higher Education Sprout Project of the National Yang Ming Chiao Tung University and Ministry of Education (MOE), Taiwan.

Conflicts of Interest: The authors declare no conflict of interest.

References

1. Al-Shahri, O.A.; Ismail, F.B.; Hannan, M.A.; Lipu, M.S.H.; Al-Shetwi, A.Q.; Begum, R.A.; Al-Muhsen, N.F.O.; Soujeri, E. Solar photovoltaic energy optimization methods, challenges and issues: A comprehensive review. *J. Clean. Prod.* **2021**, *284*, 125465. [CrossRef]
2. Hosseini, S.E.; Wahid, M.A. Hydrogen from solar energy, a clean energy carrier from a sustainable source of energy. *Int. J. Energy Res.* **2020**, *44*, 4110–4131. [CrossRef]
3. Chen, H.; Zuo, Y.; Chau, K.T.; Zhao, W.; Lee, C.H.T. Modern electric machines and drives for wind power generation: A review of opportunities and challenges. *IET Renew. Power Gener.* **2021**, *15*, 1864–1887. [CrossRef]
4. Peng, Z.; Chen, X.; Yao, L. Research status and future of hydro-related sustainable complementary multi-energy power generation. *Sustain. Futures* **2021**, *3*, 100042. [CrossRef]
5. Liu, J.; Wang, J.; Xu, C.; Jiang, H.; Li, C.; Zhang, L.; Lin, J.; Shen, Z.X. Advanced Energy Storage Devices: Basic Principles, Analytical Methods, and Rational Materials Design. *Adv. Sci.* **2018**, *5*, 1700322. [CrossRef] [PubMed]
6. Abdin, Z.; Mérida, W. Hybrid energy systems for off-grid power supply and hydrogen production based on renewable energy: A techno-economic analysis. *Energy Convers. Manag.* **2019**, *196*, 1068–1079. [CrossRef]
7. Kojima, H.; Nagasawa, K.; Todoroki, N.; Ito, Y.; Matsui, T.; Nakajima, R. Influence of renewable energy power fluctuations on water electrolysis for green hydrogen production. *Int. J. Hydrogen Energy* **2023**, *48*, 4572–4593. [CrossRef]
8. Panchenko, V.A.; Daus, Y.V.; Kovalev, A.A.; Yudaev, I.V.; Litti, Y.V. Prospects for the production of green hydrogen: Review of countries with high potential. *Int. J. Hydrogen Energy* **2023**, *48*, 4551–4571. [CrossRef]
9. Khademi, M.H.; Alipour-Dehkordi, A.; Nalchifard, F. Sustainable hydrogen and syngas production from waste valorization of biodiesel synthesis by-product: Green chemistry approach. *Renew. Sust. Energ. Rev.* **2023**, *175*, 113191. [CrossRef]
10. Liu, Y.; Zhou, D.; Deng, T.; He, G.; Chen, A.; Sun, X.; Yang, Y.; Miao, P. Research progress of oxygen evolution reaction catalysts for electrochemical water splitting. *ChemSusChem* **2021**, *14*, 5359–5383. [CrossRef]
11. Chang, C.-J.; Lai, C.-W.; Jiang, W.-C.; Li, Y.-S.; Choi, C.; Yu, H.-C.; Chen, S.-J.; Choi, Y. Fabrication and characterization of P-type semiconducting copper oxide-based thin-film photoelectrodes for solar water splitting. *Coatings* **2022**, *12*, 1206. [CrossRef]
12. Yin, T.-H.; Liu, B.-J.; Lin, Y.-W.; Li, Y.-S.; Lai, C.-W.; Lan, Y.-P.; Choi, C.; Chang, H.-C.; Choi, Y. Electrodeposition of Copper Oxides as Cost-Effective Heterojunction Photoelectrode Materials for Solar Water Splitting. *Coatings* **2022**, *12*, 1839. [CrossRef]
13. Wan, C.; Duan, X.; Huang, Y. Molecular design of single-atom catalysts for oxygen reduction reaction. *Adv. Energy Mater.* **2020**, *10*, 1903815. [CrossRef]
14. Yeh, J.W.; Chen, S.K.; Lin, S.J.; Gan, J.Y.; Chin, T.S.; Shun, T.T.; Tsau, C.H.; Chang, S.Y. Nanostructured high-entropy alloys with multiple principal elements: Novel alloy design concepts and outcomes. *Adv. Eng. Mater.* **2004**, *6*, 299–303. [CrossRef]
15. Yang, X.; Guo, R.; Cai, R.; Ouyang, Y.; Yang, P.; Xiao, J. Engineering high-entropy materials for electrocatalytic water splitting. *Int. J. Hydrogen Energy* **2022**, *47*, 13561–13578. [CrossRef]

16. Hussain, I.; Lamiel, C.; Ahmad, M.; Chen, Y.; Shuang, S.; Javed, M.S.; Yang, Y.; Zhang, K. High entropy alloys as electrode material for supercapacitors: A review. *J. Energy Storage* **2021**, *44*, 103405. [CrossRef]
17. Yeh, J.-W. Alloy Design Strategies and Future Trends in High-Entropy Alloys. *JOM* **2013**, *65*, 1759–1771. [CrossRef]
18. Lewin, E. Multi-component and high-entropy nitride coatings-A promising field in need of a novel approach. *J. Appl. Phys.* **2020**, *127*, 160901. [CrossRef]
19. Liu, C.; Zhu, H.; Lu, S.; Duan, F.; Du, M. High entropy alloy nitrides with integrated nanowire/nanosheet architecture for efficient alkaline hydrogen evolution reactions. *New J. Chem.* **2021**, *45*, 22255–22260. [CrossRef]
20. Jin, T.; Sang, X.; Unocic, R.R.; Kinch, R.T.; Liu, X.; Hu, J.; Liu, H.; Dai, S. Mechanochemical-Assisted Synthesis of High-Entropy Metal Nitride via a Soft Urea Strategy. *Adv. Mater.* **2018**, *30*, 1707512. [CrossRef]
21. Sarker, P.; Harrington, T.; Toher, C.; Oses, C.; Samiee, M.; Maria, J.-P.; Brenner, D.W.; Vecchio, K.S.; Curtarolo, S. High-entropy high-hardness metal carbides discovered by entropy descriptors. *Nat. Commun.* **2018**, *9*, 4980. [CrossRef] [PubMed]
22. Wang, D.; Liu, Z.; Du, S.; Zhang, Y.; Li, H.; Xiao, Z.; Chen, W.; Chen, R.; Wang, Y.; Zou, Y. Low-temperature synthesis of small-sized high-entropy oxides for water oxidation. *J. Mater. Chem.* **2019**, *7*, 24211–24216. [CrossRef]
23. Bérardan, D.; Franger, S.; Dragoe, D.; Meena, A.K.; Dragoe, N. Colossal dielectric constant in high entropy oxides. *Phys Status Solidi Rapid Res Lett.* **2016**, *10*, 328–333. [CrossRef]
24. Tian, Z.; Zhang, Y.; Zhang, J.; Shi, P. Facile Preparation, Microstructure and Dielectric Properties of $La(Cr_{0.2}Mn_{0.2}Fe_{0.2}Co_{0.2}Ni_{0.2})O_3$ Perovskite High-Entropy Ceramics. *Crystals* **2022**, *12*, 1756. [CrossRef]
25. Katzbaer, R.R.; dos Santos Vieira, F.M.; Dabo, I.; Mao, Z.; Schaak, R.E. Band Gap Narrowing in a High-Entropy Spinel Oxide Semiconductor for Enhanced Oxygen Evolution Catalysis. *J. Am. Chem. Soc.* **2023**, *145*, 6753–6761. [CrossRef] [PubMed]
26. Hong, W.; Chen, F.; Shen, Q.; Han, Y.-H.; Fahrenholtz, W.G.; Zhang, L. Microstructural evolution and mechanical properties of (Mg,Co,Ni,Cu,Zn)O high-entropy ceramics. *J. Am. Ceram.* **2019**, *102*, 2228–2237. [CrossRef]
27. Tang, L.; Li, Z.; Chen, K.; Li, C.; Zhang, X.; An, L. High-entropy oxides based on valence combinations: Design and practice. *J. Am. Ceram.* **2021**, *104*, 1953–1958. [CrossRef]
28. Liang, B.; Ai, Y.; Wang, Y.; Liu, C.; Ouyang, S.; Liu, M. Spinel-type $(FeCoCrMnZn)_3O_4$ high-entropy oxide: Facile preparation and supercapacitor performance. *Materials* **2020**, *13*, 5798. [CrossRef]
29. Petrovičovà, B.; Xu, W.; Musolino, M.G.; Pantò, F.; Patanè, S.; Pinna, N.; Santangelo, S.; Triolo, C. High-Entropy Spinel Oxides Produced via Sol-Gel and Electrospinning and Their Evaluation as Anodes in Li-Ion Batteries. *Appl. Sci.* **2022**, *12*, 5965. [CrossRef]
30. Xu, Y.; Xu, X.; Bi, L. A high-entropy spinel ceramic oxide as the cathode for proton-conducting solid oxide fuel cells. *J. Adv. Ceram.* **2022**, *11*, 794–804. [CrossRef]
31. Abdel-Aal, S.K.; Beskrovnyi, A.I.; Ionov, A.M.; Mozhchil, R.N.; Abdel-Rahman, A.S. Structure investigation by neutron diffraction and X-ray diffraction of graphene nanocomposite CuO-rGO prepared by low-cost method. *Phys. Status Solidi A* **2021**, *218*, 2100138. [CrossRef]
32. Xing, H.; Lei, E.; Guo, Z.; Zhao, D.; Liu, Z. Enhancement in the charge transport and photocorrosion stability of CuO photocathode: The synergistic effect of spatially separated dual-cocatalysts and p-n heterojunction. *Chem. Eng. J.* **2020**, *394*, 124907. [CrossRef]
33. Hsu, Y.-J.; Chiang, W.-C.; Wu, J.-K. Corrosion behavior of $FeCoNiCrCu_x$ high-entropy alloys in 3.5% sodium chloride solution. *Mater. Chem. Phys.* **2005**, *92*, 112–117. [CrossRef]
34. Cai, Y.; Manladan, S.M.; Luo, Z. Tribological behaviour of the double $FeCoNiCrCu_x$ middle-entropy alloy coatings. *Surf. Eng.* **2019**, *35*, 14–21. [CrossRef]
35. Wang, W.L.; Hu, L.; Luo, S.B.; Meng, L.J.; Geng, D.L.; Wei, B. Liquid phase separation and rapid dendritic growth of high-entropy CoCrCuFeNi alloy. *Intermetallics* **2016**, *77*, 41–45. [CrossRef]
36. Liu, Y.Y.; Chen, Z.; Shi, J.C.; Wang, Z.Y.; Zhang, J.Y. The effect of Al content on microstructures and comprehensive properties in $Al_xCoCrCuFeNi$ high entropy alloys. *Vacuum* **2019**, *161*, 143–149. [CrossRef]
37. Patra, S.; Munichandraiah, N. Supercapacitor studies of electrochemically deposited PEDOT on stainless steel substrate. *J. Appl. Polym. Sci.* **2007**, *106*, 1160–1171. [CrossRef]
38. Eugénio, S.; Silva, T.M.; Carmezim, M.J.; Duarte, R.G.; Montemor, M.F. Electrodeposition and characterization of nickel–copper metallic foams for application as electrodes for supercapacitors. *J. Appl. Electrochem.* **2014**, *44*, 455–465. [CrossRef]
39. Liu, X.; Xu, W.; Zheng, D.; Li, Z.; Zeng, Y.; Lu, X. Carbon cloth as an advanced electrode material for supercapacitors: Progress and challenges. *J. Mater. Chem.* **2020**, *8*, 17938–17950. [CrossRef]
40. Zhang, C.J.; Nicolosi, V. Graphene and MXene-based transparent conductive electrodes and supercapacitors. *Energy Stor. Mater.* **2019**, *16*, 102–125. [CrossRef]
41. Chiang, C.-Y.; Aroh, K.; Franson, N.; Satsangi, V.R.; Dass, S.; Ehrman, S. Copper oxide nanoparticle made by flame spray pyrolysis for photoelectrochemical water splitting-Part II. Photoelectrochemical study. *Int. J. Hydrogen Energy* **2011**, *36*, 15519–15526. [CrossRef]
42. Jian, J.; Kumar, R.; Sun, J. Cu_2O/ZnO p-n Junction Decorated with NiO_x as a Protective Layer and Cocatalyst for Enhanced Photoelectrochemical Water Splitting. *ACS Appl. Energy Mater.* **2020**, *3*, 10408–10414. [CrossRef]
43. Hossain, R.; Nekouei, R.K.; Al Mahmood, A.; Sahajwalla, V. Value-added fabrication of NiO-doped CuO nanoflakes from waste flexible printed circuit board for advanced photocatalytic application. *Sci. Rep.* **2022**, *12*, 12171. [CrossRef]
44. Liu, F.; Yang, X.; Qiao, Z.; Zhang, L.; Cao, B.; Duan, G. Highly transparent 3D NiO-Ni/Ag-nanowires/FTO micro-supercapacitor electrodes for fully transparent electronic device purpose. *Electrochim. Acta* **2018**, *260*, 281–289. [CrossRef]

45. Shaheen Shah, S.; Aziz, M.A.; Al-Betar, A.-R.; Mahfoz, W. Electrodeposition of polyaniline on high electroactive indium tin oxide nanoparticles-modified fluorine doped tin oxide electrode for fabrication of high-performance hybrid supercapacitor. *Arab. J. Chem.* **2022**, *15*, 104058. [CrossRef]
46. Ferreira, T.A.S.; Waerenborgh, J.C.; Mendonça, M.; Nunes, M.R.; Costa, F.M. Structural and morphological characterization of $FeCo_2O_4$ and $CoFe_2O_4$ spinels prepared by a coprecipitation method. *Solid State Sci.* **2003**, *5*, 383–392. [CrossRef]
47. Tunell, G.; Posnjak, E.; Ksanda, C. Geometrical and optical properties, and crystal structure of tenorite. *Z. Krist.—Cryst. Mater.* **1935**, *90*, 120–142. [CrossRef]
48. Bin Mobarak, M.; Hossain, M.S.; Chowdhury, F.; Ahmed, S. Synthesis and characterization of CuO nanoparticles utilizing waste fish scale and exploitation of XRD peak profile analysis for approximating the structural parameters. *Arab. J. Chem.* **2022**, *15*, 104117. [CrossRef]
49. Liu, X.; Chang, C.-F.; Rata, A.D.; Komarek, A.C.; Tjeng, L.H. Fe_3O_4 thin films: Controlling and manipulating an elusive quantum material. *Npj Quantum Mater.* **2016**, *1*, 16027. [CrossRef]
50. Bhargava, R.; Khan, S.; Ahmad, N.; Ansari, M.M.N. Investigation of structural, optical and electrical properties of Co_3O_4 nanoparticles. *AIP Conf. Proc.* **2018**, *1953*, 030034.
51. Zorkipli, N.N.M.; Kaus, N.H.M.; Mohamad, A.A. Synthesis of NiO Nanoparticles through Sol-gel Method. *Procedia Chem.* **2016**, *19*, 626–631. [CrossRef]
52. Wang, Y.K.; Guo, G.Y.; Jeng, H.-T. An ab initio study of the magnetocrystalline anisotropy and magnetoelastic coupling of half-metallic CrO_2. *J. Magn. Magn. Mater.* **2004**, *282*, 139–142. [CrossRef]
53. Akrami, S.; Murakami, Y.; Watanabe, M.; Ishihara, T.; Arita, M.; Fuji, M.; Edalati, K. Defective high-entropy oxide photocatalyst with high activity for CO_2 conversion. *Appl. Catal. B* **2022**, *303*, 120896. [CrossRef]
54. Yan, Z.; Li, D.; Zhang, X.; Men, Q.; Fan, B.; Guan, L.; Guo, X.; Zhang, R.; Zhao, B. Dual-phase high-entropy $(FeCoNiZn)_xV_2O_y$ oxides with promising microwave absorption properties. *Ceram. Int.* **2022**, *48*, 36871–36879. [CrossRef]
55. Edalati, P.; Wang, Q.; Razavi-Khosroshahi, H.; Fuji, M.; Ishihara, T.; Edalati, K. Photocatalytic hydrogen evolution on a high-entropy oxide. *J. Mater. Chem.* **2020**, *8*, 3814–3821. [CrossRef]
56. Rodríguez-Carvajal, J. FullProf. *CEA/Saclay Fr.* **2001**, *1045*, 132–146.
57. Grazulis, S.; Chateigner, D.; Downs, R.T.; Yokochi, A.F.T.; Quiros, M.; Lutterotti, L.; Manakova, E.; Butkus, J.; Moeck, P.; Le Bail, A. Crystallography Open Database—An open-access collection of crystal structures. *J. Appl. Crystallogr.* **2009**, *42*, 726–729. [CrossRef]
58. Jain, S.; Shah, J.; Negi, N.S.; Sharma, C.; Kotnala, R.K. Significance of interface barrier at electrode of hematite hydroelectric cell for generating ecopower by water splitting. *Int. J. Energy Res.* **2019**, *43*, 4743–4755. [CrossRef]
59. Zhang, X.; Liu, X.; Zeng, Y.; Tong, Y.; Lu, X. Oxygen Defects in Promoting the Electrochemical Performance of Metal Oxides for Supercapacitors: Recent Advances and Challenges. *Small Methods* **2020**, *4*, 1900823. [CrossRef]
60. Chen, H.; Qiu, N.; Wu, B.; Yang, Z.; Sun, S.; Wang, Y. A new spinel high-entropy oxide $(Mg_{0.2}Ti_{0.2}Zn_{0.2}Cu_{0.2}Fe_{0.2})_3O_4$ with fast reaction kinetics and excellent stability as an anode material for lithium ion batteries. *RSC Adv.* **2020**, *10*, 9736–9744. [CrossRef]
61. Bui, N.T.; Kang, H.; Teat, S.J.; Su, G.M.; Pao, C.-W.; Liu, Y.-S.; Zaia, E.W.; Guo, J.; Chen, J.-L.; Meihaus, K.R.; et al. A nature-inspired hydrogen-bonded supramolecular complex for selective copper ion removal from water. *Nat. Commun.* **2020**, *11*, 3947. [CrossRef] [PubMed]
62. Karikalan, N.; Karthik, R.; Chen, S.-M.; Karuppiah, C.; Elangovan, A. Sonochemical Synthesis of Sulfur Doped Reduced Graphene Oxide Supported CuS Nanoparticles for the Non-Enzymatic Glucose Sensor Applications. *Sci. Rep.* **2017**, *7*, 2494. [CrossRef] [PubMed]
63. Wang, D.; Jiang, S.; Duan, C.; Mao, J.; Dong, Y.; Dong, K.; Wang, Z.; Luo, S.; Liu, Y.; Qi, X. Spinel-structured high entropy oxide $(FeCoNiCrMn)_3O_4$ as anode towards superior lithium storage performance. *J. Alloys Compd.* **2020**, *844*, 156158. [CrossRef]
64. Alex, C.; Sarma, S.C.; Peter, S.C.; John, N.S. Competing Effect of Co^{3+} Reducibility and Oxygen-Deficient Defects Toward High Oxygen Evolution Activity in Co_3O_4 Systems in Alkaline Medium. *ACS Appl. Energy Mater.* **2020**, *3*, 5439–5447. [CrossRef]
65. Nguyen, T.X.; Patra, J.; Chang, J.-K.; Ting, J.-M. High entropy spinel oxide nanoparticles for superior lithiation-delithiation performance. *J. Mater. Chem.* **2020**, *8*, 18963–18973. [CrossRef]
66. Rajan, A.; Sharma, M.; Sahu, N.K. Assessing magnetic and inductive thermal properties of various surfactants functionalised Fe_3O_4 nanoparticles for hyperthermia. *Sci. Rep.* **2020**, *10*, 15045. [CrossRef]
67. Xiao, B.; Wu, G.; Wang, T.; Wei, Z.; Sui, Y.; Shen, B.; Qi, J.; Wei, F.; Zheng, J. High-entropy oxides as advanced anode materials for long-life lithium-ion Batteries. *Nano Energy.* **2022**, *95*, 106962. [CrossRef]
68. Cabanel, R.; Barral, G.; Diard, J.P.; Le Gorrec, B.; Montella, C. Determination of the diffusion coefficient of an inserted species by impedance spectroscopy: Application to the $H/H_xNb_2O_5$ system. *J. Appl. Electrochem.* **1993**, *23*, 93–97. [CrossRef]
69. Ramya, R.; Sivasubramanian, R.; Sangaranarayanan, M.V. Conducting polymers-based electrochemical supercapacitors-Progress and prospects. *Electrochim. Acta* **2013**, *101*, 109–129. [CrossRef]
70. Mishra, D.; Kim, S.; Kumar, N.; Krishnaiah, M.; Jin, S.H. Self-discharge mitigated supercapacitors via hybrid CuO-nickel sulfide heterostructure for energy efficient, wireless data storage application. *J. Mater. Sci. Technol.* **2023**, *147*, 77–90. [CrossRef]
71. Nguyen, T.X.; Tsai, C.-C.; Patra, J.; Clemens, O.; Chang, J.-K.; Ting, J.-M. Co-free high entropy spinel oxide anode with controlled morphology and crystallinity for outstanding charge/discharge performance in Lithium-ion batteries. *Chem. Eng. J.* **2022**, *430*, 132658. [CrossRef]

72. Patra, J.; Nguyen, T.X.; Tsai, C.-C.; Clemens, O.; Li, J.; Pal, P.; Chan, W.K.; Lee, C.-H.; Chen, H.-Y.T.; Ting, J.-M.; et al. Effects of Elemental Modulation on Phase Purity and Electrochemical Properties of Co-free High-Entropy Spinel Oxide Anodes for Lithium-Ion Batteries. *Adv. Funct. Mater.* **2022**, *32*, 2110992. [CrossRef]
73. Mahmood, A.; Tezcan, F.; Kardaş, G. Photoelectrochemical characteristics of CuO films with different electrodeposition time. *Int. J. Hydrogen Energy* **2017**, *42*, 23268–23275. [CrossRef]
74. Yadav, P.; Manivannan, S.; Kim, H.-S.; Pandey, K.; Kim, K.; Kim, J. Electrochemical Properties of Highly Sensitive and Selective CuO Nanostructures Based Neurotransmitter Dopamine Sensor. *Electroanalysis* **2017**, *29*, 2106–2113. [CrossRef]
75. Bredar, A.R.C.; Chown, A.L.; Burton, A.R.; Farnum, B.H. Electrochemical Impedance Spectroscopy of Metal Oxide Electrodes for Energy Applications. *ACS Appl. Energy Mater.* **2020**, *3*, 66–98. [CrossRef]
76. Uke, S.J.; Mardikar, S.P.; Bambole, D.R.; Kumar, Y.; Chaudhari, G.N. Sol-gel citrate synthesized Zn doped $MgFe_2O_4$ nanocrystals: A promising supercapacitor electrode material. *Mater. Sci.* **2020**, *3*, 446–455. [CrossRef]
77. Ansari, M.S.; Kim, H. Enhanced electrocatalytic oxygen evolution reaction kinetics using dual-phase engineering of self-supported hierarchical $NiCoV(OH)_x$ nanowire arrays. *Fuel* **2021**, *304*, 121309. [CrossRef]
78. Allagui, A.; Freeborn, T.J.; Elwakil, A.S.; Maundy, B.J. Reevaluation of Performance of Electric Double-layer Capacitors from Constant-current Charge/Discharge and Cyclic Voltammetry. *Sci. Rep.* **2016**, *6*, 38568. [CrossRef]
79. Adewinbi, S.A.; Taleatu, B.A.; Busari, R.A.; Maphiri, V.M.; Oyedotun, K.O.; Manyala, N. Synthesis and electrochemical characterization of pseudocapacitive α-MoO_3 thin film as transparent electrode material in optoelectronic and energy storage devices. *Mater. Chem. Phys.* **2021**, *264*, 124468. [CrossRef]
80. Huang, J.; Sullivan, N.P.; Zakutayev, A.; O'Hayre, R. How reliable is distribution of relaxation times (DRT) analysis? A dual regression-classification perspective on DRT estimation, interpretation, and accuracy. *Electrochim. Acta* **2023**, *443*, 141879. [CrossRef]
81. Ciucci, F.; Chen, C. Analysis of Electrochemical Impedance Spectroscopy Data Using the Distribution of Relaxation Times: A Bayesian and Hierarchical Bayesian Approach. *Electrochim. Acta* **2015**, *167*, 439–454. [CrossRef]
82. Effat, M.B.; Ciucci, F. Bayesian and Hierarchical Bayesian Based Regularization for Deconvolving the Distribution of Relaxation Times from Electrochemical Impedance Spectroscopy Data. *Electrochim. Acta* **2017**, *247*, 1117–1129. [CrossRef]
83. Wan, T.H.; Saccoccio, M.; Chen, C.; Ciucci, F. Influence of the Discretization Methods on the Distribution of Relaxation Times Deconvolution: Implementing Radial Basis Functions with DRTtools. *Electrochim. Acta* **2015**, *184*, 483–499. [CrossRef]
84. Wu, Y.; Liu, D.; Zhuang, H.; Le, J.; Kuang, Y. High-performance bulk heterojunction-based photocathode with facile architecture for photoelectrochemical water splitting. *Chin. Chem. Lett.* **2023**, *34*, 107480. [CrossRef]
85. Schutjajew, K.; Tichter, T.; Schneider, J.; Antonietti, M.; Roth, C.; Oschatz, M. Insights into the sodiation mechanism of hard carbon-like materials from electrochemical impedance spectroscopy. *Phys. Chem. Chem. Phys.* **2021**, *23*, 11488–11500. [CrossRef]
86. Attias, R.; Vijaya Sankar, K.; Dhaka, K.; Moschkowitsch, W.; Elbaz, L.; Caspary Toroker, M.; Tsur, Y. Optimization of Ni-Co-Fe-Based Catalysts for Oxygen Evolution Reaction by Surface and Relaxation Phenomena Analysis. *ChemSusChem* **2021**, *14*, 1737–1746. [CrossRef] [PubMed]
87. Li, P.; Wang, Y.; Du, X.; Zhang, X. Promoted electrocatalytic water splitting by regulating the concentration of oxygen vacancies. *Int. J. Hydrogen Energy*, 2023; *in press*. [CrossRef]
88. Song, Z.; Wang, K.; Sun, Q.; Zhang, L.; Li, J.; Li, D.; Sze, P.W.; Liang, Y.; Sun, X.; Fu, X.Z. High-Performance Ammonium Cobalt Phosphate Nanosheet Electrocatalyst for Alkaline Saline Water Oxidation. *Adv. Sci.* **2021**, *8*, 2100498. [CrossRef]
89. Liu, X.; Cui, S.; Sun, Z.; Ren, Y.; Zhang, X.; Du, P. Self-supported copper oxide electrocatalyst for water oxidation at low overpotential and confirmation of its robustness by Cu K-edge X-ray absorption spectroscopy. *J. Phys. Chem.* **2016**, *120*, 831–840. [CrossRef]
90. Hong, Y.R.; Kim, K.M.; Ryu, J.H.; Mhin, S.; Kim, J.; Ali, G.; Chung, K.Y.; Kang, S.; Han, H. Dual-phase engineering of nickel boride-hydroxide nanoparticles toward high-performance water oxidation electrocatalysts. *Adv. Funct. Mater.* **2020**, *30*, 2004330. [CrossRef]
91. Ran, J.; Wu, J.-F.; Hu, Y.; Shakouri, M.; Xia, B.; Gao, D. Atomic-level coupled spinel@ perovskite dual-phase oxides toward enhanced performance in Zn-air batteries. *J. Mater. Chem.* **2022**, *10*, 1506–1513. [CrossRef]
92. Einert, M.; Waheed, A.; Lauterbach, S.; Mellin, M.; Rohnke, M.; Wagner, L.Q.; Gallenberger, J.; Tian, C.; Smarsly, B.M.; Jaegermann, W. Sol-Gel-Derived Ordered Mesoporous High Entropy Spinel Ferrites and Assessment of Their Photoelectrochemical and Electrocatalytic Water Splitting Performance. *Small* **2023**, *19*, 2205412. [CrossRef] [PubMed]
93. Beere, H.K.; Kulkarni, P.; Maiti, U.N.; Balakrishna, R.G.; Mukherjee, P.; Jung, H.Y.; Samanta, K.; Ghosh, D. Realizing Favourable Oxygen Electrocatalytic Activity with Compositionally Complex Metal Molybdates. *Sustain. Energy Fuels* **2023**. [CrossRef]